

Characterization of the $^{12}\text{C}(\text{p},\text{p}')^{12}\text{C}$ Reaction ($E_p=19.5\text{--}30$ MeV) for Active Interrogation

J. Nattress^{1,2}, F. Sutanto¹, P.-W. Fang³, Y.-Z. Chen³, A. Cheng³,
K.-Y. Chu⁴, T.-S. Duh⁴, H.-Y. Tsai³, M.-W. Lin^{3,*} and I. Jovanovic¹

¹*Department of Nuclear Engineering and Radiological Sciences,
University of Michigan, Ann Arbor, MI 48109 USA*

²*Oak Ridge National Laboratory, Oak Ridge, TN 37830 USA*

³*Institute of Nuclear Engineering and Science, National Tsing Hua University, Hsinchu 30013, Taiwan and*

⁴*Isotope Application Division, Institute of Nuclear Energy Research, Taoyuan City 32546, Taiwan*

(Dated: November 14, 2019)

Passive detection of special nuclear material (SNM) is challenging due to its inherently low rate of spontaneous emission of penetrating radiation, the relative ease of shielding, and the fluctuating and frequently overwhelming background. Active interrogation (AI), the use of external radiation to increase the emission rate of characteristic radiation from SNM, has long been considered to be a promising method to overcome those challenges. Current AI systems that incorporate radiography tend to use bremsstrahlung beams, which can deliver high radiation doses. Low-energy ion-driven nuclear reactions that produce multiple monoenergetic photons may be used as an alternative. The $^{12}\text{C}(\text{p},\text{p}')^{12}\text{C}$ is one such reaction that could produce large gamma-ray yields of highly penetrating 4.4- and 15.1-MeV gamma rays. This reaction does not directly produce neutrons below the ~ 19.7 -MeV threshold, and the 15.1-MeV gamma-ray line is well matched to the photofission cross section of ^{235}U and ^{238}U . We report the measurements of thick-target gamma-ray yields at 4.4 and 15.1 MeV from the $^{12}\text{C}(\text{p},\text{p}')^{12}\text{C}$ at proton energies of 19.5, 25, and 30 MeV. Measurements were made with two 3" EJ309 cylindrical liquid scintillation detectors and thermoluminescent dosimeters placed at 0° and 90° , with an additional 1.5" NaI(Tl) cylindrical scintillation detector at 0° . We estimate the highest yields of the 4.4- and 15.1-MeV gamma rays of $1.65 \times 10^{10} \text{ sr}^{-1} \mu\text{C}^{-1}$ and $4.47 \times 10^8 \text{ sr}^{-1} \mu\text{C}^{-1}$ at a proton energy of 30 MeV, respectively. The yield of 4.4 and 15.1 MeV gamma rays in all experimental configurations is greater than a comparable deuteron-driven reaction that produces the same gamma-ray energies – $^{11}\text{B}(\text{d},\text{n}\gamma)^{12}\text{C}$. However, a two orders of magnitude increase of the neutron radiation dose is observed when the proton energy increases from 19.5 to 30 MeV.

I. INTRODUCTION

A significant nuclear security concern is the screening and interdiction of shielded SNM, which includes cargo containers, even smaller objects, and movement of illicit materials into and out of enrichment facilities [1, 2]. Over several million ocean cargo containers arrive at United States seaports annually [3, 4] with over half the distribution of incoming containers concentrated at three ports—Los Angeles, Long Beach, and New York [3]. This uneven distribution raises serious concerns about the number of containers that can be accurately scanned without impeding commerce and still maintaining nuclear security vigilance.

The technique of active interrogation (AI) has been of increasing interest in recent years for detecting special nuclear material (SNM) [5]. This is based on an expectation that the increased magnitude and the time structure of the fission signatures imposed by AI can also increase the probability of SNM detection. New and innovative approaches are needed to overcome specific AI application constraints, such as the maximum scanning time and radiation dose. Traditional AI systems tend to employ energetic X-ray transmission radiography us-

ing continuous-energy-spectrum bremsstrahlung beams. Such beams can deliver high radiation doses, especially at high electron energies needed to produce sufficiently energetic photons for penetrating radiography and inducing photofission. The lower-energy photons present in the bremsstrahlung spectrum, well below the photofission threshold, have poor penetration through dense objects and may significantly contribute to the imparted radiation dose without inducing fission [6, 7]. As a result, an alternative method for production of quasi-monoenergetic, continuously tunable high-energy X-rays that has garnered considerable attention in the recent period is inverse Compton scattering [8].

Low-energy ion-driven nuclear reactions that produce multiple monoenergetic, high-energy gamma rays could also be used as an alternative to bremsstrahlung in AI applications. Reactions that exhibit a large positive Q -value allow the use of lower-energy (and thus typically smaller and simpler) accelerators to create highly penetrating energetic photons. Such monoenergetic or multiple-monoenergetic AI sources may offer benefits such as improved performance in radiography and higher fission rates per unit of radiation dose. Near monoenergetic photon sources at or near the photo-fission resonance (~ 15 MeV) offer a factor of 4 lower imparted radiation dose for a bremsstrahlung source with a 19 MeV endpoint energy [6]. Low-energy nuclear reactions, therefore, represent a promising method to produce

* mwlin@mx.nthu.edu.tw

quasi-monoenergetic photon beams which could lead to construction of lower-dose, small-footprint systems to detect illicit movement of SNM as well as support a broad range of measurements in the area of nuclear security, nuclear nonproliferation, and nuclear safety.

Figure 1 illustrates a conceptual design of one specific application – a cargo screening AI system – where a low energy nuclear reaction source could be used to increase the scanning rate of cargo containers by implementing simultaneous scanning of multiple cargo streams. Such a system must address some of the major specifications for cargo container scanning such as an acceptable radiation dose imparted to the cargo, penetration capability of the AI source, container scanning speed, and material discrimination [9].

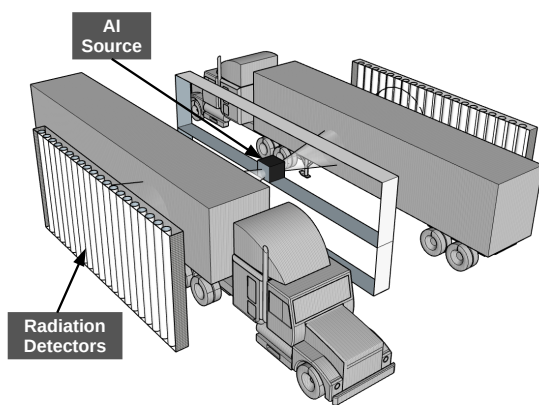


FIG. 1: Conceptual design of a cargo scanning system using a low-energy nuclear reaction based AI source, where a single source may be used to implement simultaneous scanning of multiple cargo streams [10].

Several candidate reactions have been previously identified that produce prolific yields of energetic gamma rays, including those above the photofission energy threshold, or neutrons that may also be viable for AI interrogation [11]. Such high-energy particles can be used to penetrate dense cargo to perform transmission radiography for material identification [12–14] or induce fission [15, 16]. In Ref. [11] several candidate reactions were considered, including (p,γ) , $(p,\alpha\gamma)$, and $(d,n\gamma)$. Four candidate targets (^{11}B , ^7Li , ^{19}F , and ^{15}N) were selected based on the reaction Q -values and gamma-ray energies from the resulting excited nuclei. Protons, deuterons, and tritons were used as projectiles. The $^{11}\text{B}(d,n)^{12}\text{C}$ reaction ($Q=13.6$ MeV) has emerged as one of the leading candidates for an AI source [17]. With deuteron energies of several MeV or higher, this reaction produces a strong 15.1-MeV gamma-ray energy line that is well overlapped with the photofission cross section of ^{235}U and ^{238}U [18]. This reaction, however, has a high neutron yield, approximately 20–50 times the relevant gamma-ray yield [12].

With the continued advancement of superconducting

cyclotron technology, more compact, deployable AI systems utilizing nuclear reactions that do not directly produce neutrons with Q -values ≤ 0 can be envisioned. One such reaction which can excite the 15.1-MeV state of ^{12}C inelastically is $^{12}\text{C}(p,p')^{12}\text{C}$ [19–22]. This reaction has an incident proton threshold energy of 16.39 MeV for exciting the 15.1-MeV ^{12}C state and does not directly produce neutrons below the ~ 19.6 -MeV threshold [23, 24]. Gamma rays at 4.4 MeV are also produced prolifically in this reaction, and can be used in conjunction with 15.1-MeV gamma rays to perform spectroscopic transmission radiography and identify the atomic number of an unknown material [12, 13].

Organic scintillation detectors are typically used to perform fast neutron spectroscopy, where pulse-shape analysis enables the discrimination between neutrons and photons. While it is well-known that low- Z organic scintillators are also sensitive to photons and their response is nearly proportional, photon spectroscopy is usually not attempted due to low efficiency, resolution, and the absence of photopeak features in the light-output spectrum. Although the presence of prominent full-energy deposition peaks is often favored for photon spectroscopy, many common high- Z scintillators depend on expensive crystalline materials with slow decay time characteristics, which perform poorly in high-rate environments. They can also be costly to scale to large volumes, or may not be able to distinguish between neutron and photon interactions. The fast rise-time and decay-time response of organic liquid scintillator, along with the ability to detect and identify both neutrons and photons, makes it an attractive choice for an AI system that requires simultaneous photons and neutron identification in a mixed-radiation high-rate environment. If the photon source has a spectrum that features well-separated discrete energies, discernible spectral features can be observed in the resulting light-output spectrum, which can be exploited to perform spectroscopy [10].

We present gamma-ray yield measurements of the $^{12}\text{C}(p,p')^{12}\text{C}$ reaction made with two organic liquid scintillators placed at 0° and 90° with respect to the proton beam axis, with an additional $\text{Na}(\text{Tl})$ detector placed at 0° for experimental validation. We further report neutron and gamma ray dose measurements. We observe an increase in the production rate of gamma rays with an increase in proton energy, as well as a rapid increase in the measured neutron radiation dose with proton energy. The AI source proposed in this work focuses on the key performance parameters—the emitted radiation flux, energy spectrum, and dose rate. Other essential design considerations such as radiation shielding requirements must be considered before final implementation.

II. MATERIALS AND METHODS

The experiments were conducted using the cyclotron located at the Institute of Nuclear Energy Research in

Taiwan. This accelerator produces proton pulses at a fixed frequency of 73.2 MHz, and the proton energy can be adjusted from 15 to 30 MeV with a maximum average current of 10 μ A delivered to the experimental station. A 6.35-mm-thick natural carbon target consisting of 98.9% ^{12}C and 1.1% ^{13}C and an active area of 2 cm \times 2 cm was held by an aluminum mount and placed at the center of an aluminum vacuum chamber (20 cm \times 20 cm \times 20 cm, 1.2 cm-thick). To prevent protons from striking the target mount and generating neutrons at the target location, a 1-cm-thick aluminum collimator was inserted into the upstream beamline for shaping the incident proton beam to a transverse diameter of 1 cm before entering the target chamber. This collimation, however, inevitably produces additional neutrons when protons in the outer radial region of each pulse strike the aluminum collimator. Therefore, a water tank (1 m \times 1 m \times 1 m) was placed to surround the vacuum pipe for shielding neutrons emitted from the collimator, such that these neutrons can be absorbed before reaching the edge of the 50-cm-thick layer of water. The on-target proton current was calibrated when the target mount was replaced by a Faraday cup, whose output was connected to a digital picoammeter (Keithley, model 486) capable of measuring currents with a resolution of 10 fA.

The radiation produced by the source was measured with one NaI(Tl) scintillation detector, two EJ309 organic liquid scintillation detectors [25], and pairs of thermoluminescent dosimeters (TLDs). The NaI(Tl) detector were placed at 0° at a distance of 2.05 m from the carbon target, while the EJ309 liquid scintillation detectors and TLDs were placed at 0° and 90° , at the same distance of 1.4 m. Here, the angles are given with respect to the propagation axis of protons incident on the target. The NaI(Tl) dimensions were 1.5" (diameter) \times 1.5" (height); the EJ309 detectors were 3" in diameter \times 3" in height. Figure 2 shows a diagram of the experimental setup including the aluminum collimator, vacuum target chamber, water tank for neutron shielding, one NaI(Tl) scintillation detector, two EJ309 liquid scintillators, and two paired TLDs. Table I summarizes the positions and

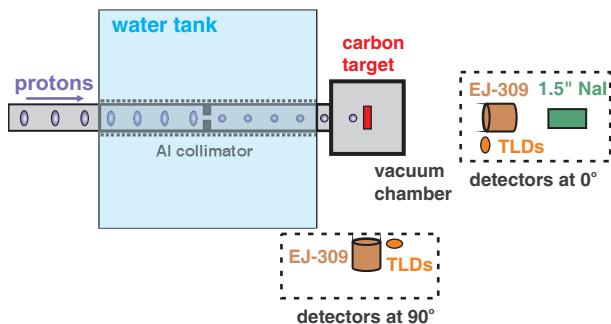


FIG. 2: Schematic of the experimental setup

solid angles subtended by detectors, as measured relative to the target. The detectors were placed at nearly the

same heights as the target height (1.5 m above the ground level). Three proton-projectile-target configurations were

TABLE I: Summary of characteristics of the scintillation detectors and their placement relative to the target

Angle	Detector	Radial Distance (m)	Height (m)	Solid Angle (sr)
0°	1.5" \times 1.5" NaI(Tl)	2.05	1.53	2.7×10^{-4}
	3" \times 3" EJ309	1.4	1.45	2.3×10^{-3}
90°	3" \times 3" EJ309	1.4	1.2	2.3×10^{-3}

tested. The compact superconducting cyclotron was operated at 0.35 nA, 0.3 nA, and 0.33 nA on-target current with 19.5 MeV, 25 MeV, and 30 MeV proton energies incident onto the carbon target, respectively. At each proton energy data were recorded for 8 hours.

Signals generated by the scintillation detectors were digitized using an 8-channel, 14-bit, 500-MHz waveform digitizer (CAEN DT5730) with a 992-ns long temporal length for all of the recorded waveforms. The CAEN Multi-Parameter Spectroscopy Software (CoMPASS) [26] was used to record the integrated charge in two distinct time windows measured with respect to the pulse trigger. We refer to these two recorded quantities as the long-gate integral (Q_{long}) and the short-gate integral (Q_{short}). Pulse-shape analysis was performed on the digitizer field-programmable gate array by calculating the pulse shape parameter (PSP) for each signal waveform, defined as

$$PSP = (Q_{long} - Q_{short}) / Q_{long}. \quad (1)$$

For the NaI(Tl) detectors, Q_{long} and Q_{short} were defined as the total charge in the time windows $[t_s, t_s + 400 \text{ ns}]$ and $[t_s, t_s + 100 \text{ ns}]$, respectively, with the reference delay $t_s = 50 \text{ ns}$ after the leading edge trigger. The time windows for the EJ309 detectors were $[t_s + 400 \text{ ns}]$ and $[t_s + 54 \text{ ns}]$ for Q_{long} and Q_{short} , respectively, where the trigger delay was set to $t_s = 10 \text{ ns}$. By performing the fiducial cut in the PSP-light output parameter space of the EJ309 response, single-photon events can be distinguished from both neutron and pile-up events. A PSP-light output scatter plot with the fiducial cuts (red) for one of the EJ309 detectors and the NaI(Tl) detector is shown in Fig. 3 and Fig. 4. Also in Fig. 3, the neutron light-output response for 19.5-, 25-, and 30-MeV protons incident on a natural carbon target is shown indicating an increase in neutron energy with increasing incident proton energy.

Fiducial cuts were used to select photon and reject pileup events, and events within the respective cuts were used to produce the photon light-output distributions for each detector for three proton-projectile-target experimental configurations. Figure 5 shows a representative photon light-output distribution which corresponds to the EJ309 detector response at 90° at a proton energy of

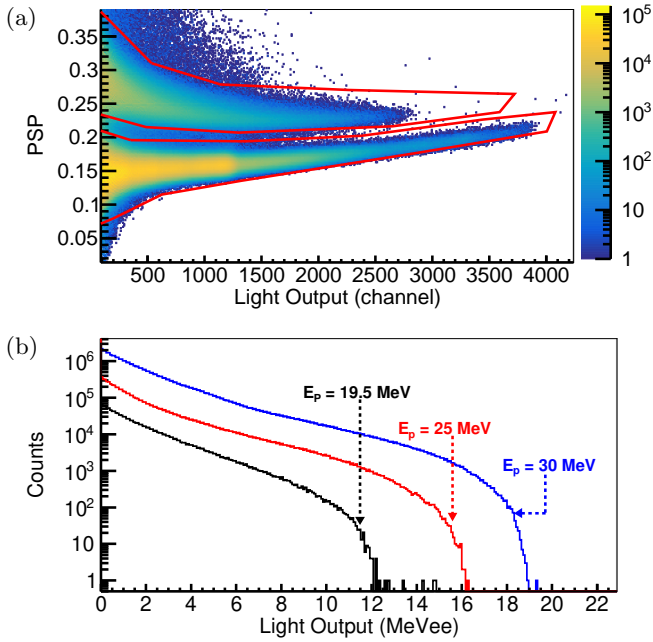


FIG. 3: (a) Response of a 3'' EJ309 detector for 19.5-MeV protons with the neutron (higher PSP) and photon (lower PSP) fiducial cuts shown in red and (b) the neutron light-output response for 19.5-, 25-, and 30-MeV protons incident on a natural carbon target for a 8-hour measurement time.

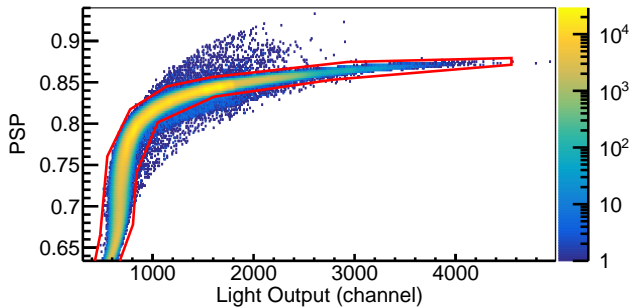


FIG. 4: Response of a 1.5'' NaI(Tl) detector for 19.5-MeV protons incident on a natural carbon target for an 8-hour measurement time. The photon fiducial cut is shown in red.

25 MeV. In Fig. 5 the double-escape peaks from 4.4-MeV and 15.1-MeV gamma rays are readily observable, along with the Compton-scattering feature at 4.4 MeV [27]. As expected, there is no observable photopeak due to the low atomic number of liquid scintillation detector's constituents. The broad energy distribution at high light output ($\gtrsim 20$ MeVee) is attributed to showering muons. The continuum between the 4.4-MeV and 15.1-MeV spectral features is attributed to bremsstrahlung photons produced by high-energy protons incident on the aluminum collimator placed upstream from the target; this is corroborated by simulation as discussed in Sect. III.

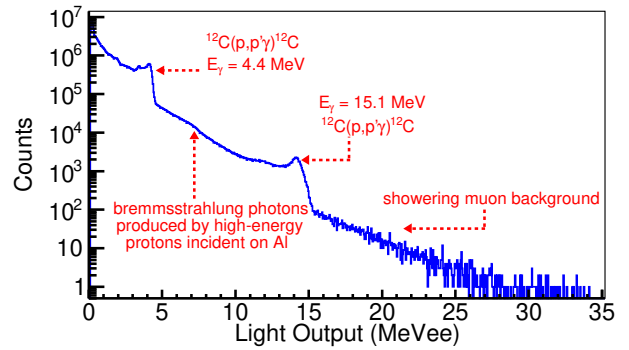


FIG. 5: Recorded light-output spectra measured with a 3'' EJ309 detector at 90° over a measurement time of 8 hours for a proton energy of 25 MeV incident on a natural carbon target.

Photon and neutron radiation doses at 0° and 90° were measured and distinguished from each other based on the dual-TLD method [28]. In this method, pairs of TLD 600 and TLD 700 chips ($3.2 \times 3.2 \times 0.89$ mm, Harshaw) were placed at the distance 1.4 m away from the carbon target at each angle. The TLD 700 is primarily sensitive to photons, since 99.993% of its lithium isotope content is ^7Li , which exhibits a much lower neutron response than that of ^6Li . In contrast, the 95.62% enrichment of ^6Li in TLD 600 allows it to record the dose contributed from both neutrons and photons. By placing paired TLDs in a mixed photon-neutron field, the TLD 600 reading Q_6 accounts for the majority of neutron response reading $Q_{6,n}$ and the minority of photon response reading $Q_{6,p}$; while the TLD 700 reading Q_7 is dominated by the photon response reading $Q_{7,p}$ when compared to the neutron response reading $Q_{7,n}$.

In our experiments, the total reading Q_6 and Q_7 measured at a given proton energy is averaged from three TLD chips of each type placed at each angle, which also allows for consistency checks. Note that, when TLD 600 and TLD 700 are placed at the same position, the measured $Q_{6,p}$ and $Q_{7,p}$ represent the same photon dose. This photon dose D_{ph} can be calibrated as

$$D_{ph} = Q_{x,p} \times CF_{x,p}, \quad (2)$$

where $CF_{x,p}$ stands for the calibration factor and $x = \{6, 7\}$ relates to TLD 600 and TLD 700, respectively. These calibration factors were measured to be $CF_{6,p} \sim 1.6 \times 10^{-5}$ mGy/nC and $CF_{7,p} \sim 1.8 \times 10^{-5}$ mGy/nC using the ^{137}Cs field established in a dedicated calibration setup. Once the photon dose D_{ph} is determined from the TLD 700 measurements, the photon response $Q_{6,p}$ of TLD 600 included in the total reading Q_6 can be estimated by

$$Q_{6,p} = D_{ph}/CF_{6,p}, \quad (3)$$

since TLD 600 experiences the same D_{ph} as the paired TLD 700. As a result, the neutron response reading $Q_{6,n}$

of the TLD 600 is determined from

$$Q_{6,n} = Q_6 - Q_{6,p}. \quad (4)$$

The TLD 600 chips were calibrated using a ^{252}Cf source, yielding a factor $CF_{H,n} \sim 2 \times 10^{-5}$ mSv/nC, which relates the neutron response $Q_{6,n}$ to the neutron dose equivalent H_n (mSv):

$$H_n = CF_{H,n} \times Q_{6,n}. \quad (5)$$

III. LIGHT-OUTPUT SPECTRUM SIMULATION

Monte Carlo simulations were performed using Geant4.10.3 [29] to help assess the spectral features in the recorded photon light-output distributions. The physics list QGSP_BERT_HP is used to model the particle interactions. The model includes the carbon target, vacuum chamber, collimator, water tank, and the surrounding concrete wall; in this way, the effect of shielding and the production of bremsstrahlung can be investigated and applied when analyzing the experimental results.

To investigate the continuum observed in the 5–10 MeV energy range, a simulation of high-energy proton interactions in a 1-cm-thick aluminum slab was performed. Bremsstrahlung photons propagate through the water tank and their energies are tallied. The softened spectrum is then used to sample the energy of a new group of photons, for which the direction of propagation is biased towards the detector. The simulated detector response to the bremsstrahlung is obtained and smeared with the resolution function. The resolution is parameterized as outlined in Ref. [27]. Monte Carlo simulations of high-energy gamma-ray (4.4 and 15.1 MeV) interactions in the EJ309 detectors have also been performed to obtain the responses of individual detectors used in the experiments.

To calculate the gamma-ray yields at 4.4 and 15.1 MeV, four individual spectra – measured background, simulated response to bremsstrahlung at the respective proton energy, and the simulated responses to 4.4 and 15.1 MeV photons – are fit to the measured data. A χ^2 -analysis was used to determine the parameters that maximize the agreement between the measured and the simulated detector responses. Local function minimization was performed using MIGRAD, HESSE, and MINOS algorithms as implemented in the ROOT framework [30]. This analysis was conducted for each detector at each of the three proton energies. The resulting fit spectra were used to calculate the yields of 4.4- and 15.1-MeV gamma rays normalized to the solid angle and measured cyclotron current. The gamma-ray yields measured with the EJ309 detectors are reported in Tables II (4.4 MeV) and III (15.1 MeV), with the NaI(Tl) detector producing results similar to the EJ309 detector at 0° .

The simulated EJ309 light output responses to 4.4-MeV gamma rays, 15.1-MeV gamma rays, and

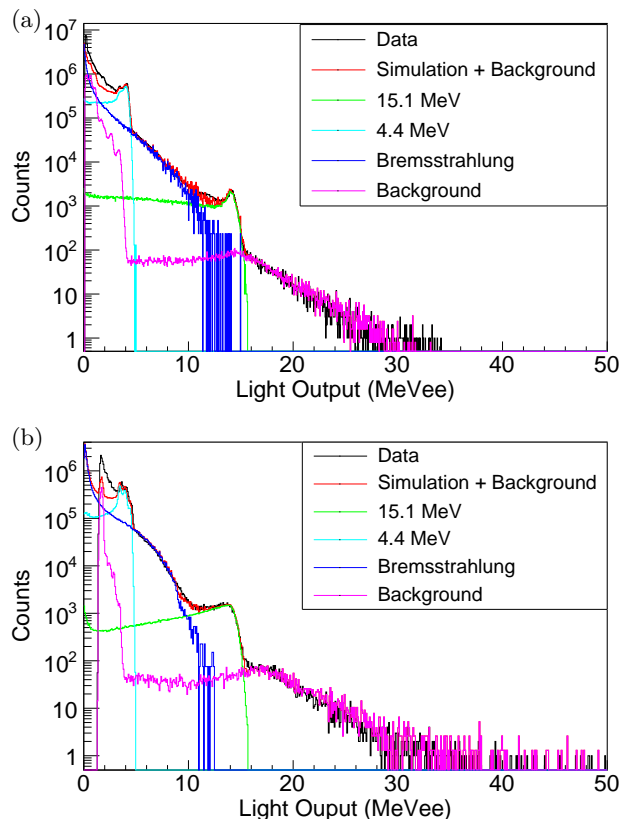


FIG. 6: Individual combined simulated and experimental fit contributions for (a) 3'' EJ309 detector detector at 90° and (b) 2'' NaI(Tl) detector detector at 0° for a 25-MeV proton incident onto a thick natural carbon target over a measurement time of 8 hours.

bremsstrahlung are scaled and added to the background spectrum such that their sum matches the experimental light output response. Individual contributions to the simulated spectra, the combined simulated spectra, and the experimental spectra for the EJ309 detector detector at 90° and the NaI(Tl) detector detector at 0° are shown in Fig. 6. In this example, protons ($E_p = 25$ MeV) are incident onto a thick natural carbon target over a measurement time of 8 hours. The final combined fit for one of the experimental configurations for the NaI(Tl) detector and EJ309 detector is shown in Fig. 7. The fit spectra show good agreement over the broad light-output range of interest.

By calculating the area under the simulated detector response for the individual contributions of 15.1- and 4.4-MeV gamma rays and knowing the on-target current used during the experiment, the absolute detection efficiency obtained from the simulation, and the experimental measurement time, we estimate the production rates of 4.4- and 15.1-MeV gamma rays. Pileup corrections have been applied to the production yields in accordance with the procedure outlined in Ref. [13].

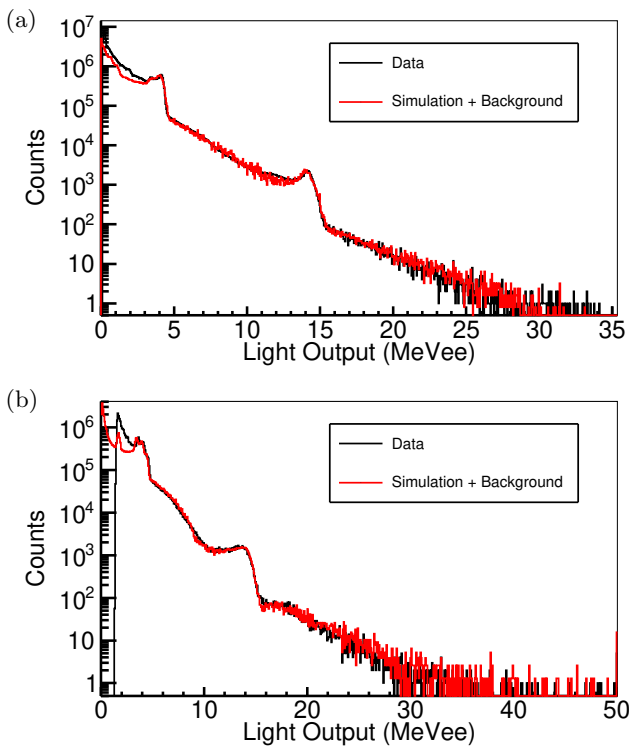


FIG. 7: Recorded light-output spectra measured with a (a) 3'' EJ309 detector detector at 90° and (b) 2'' NaI(Tl) detector detector at 0° for a 25-MeV proton incident onto a thick natural carbon target over a measurement time of 8 hours.

IV. RESULTS & DISCUSSION

The results show the expected trend: as the energy of the protons is increased, the yield of high-energy gamma rays increases. The 15.1-MeV gamma-ray yield at 0° from $^{12}\text{C}(p,p')^{12}\text{C}$ reaction is a factor of 1.3, 14.8, and 55.5 ($\text{sr}^{-1} \mu\text{C}^{-1}$) greater at proton energies of 19.5, 25, and 30 MeV, respectively, than the yield of 15.1-MeV gamma rays from $^{11}\text{B}(d,n)^{12}\text{C}$ reaction at 0° angle with 3-MeV deuteron energy [12]. The increase in the 15.1-MeV gamma-ray yield measured at 90° is even greater compared to the $^{11}\text{B}(d,n)^{12}\text{C}$ reaction. A summary of 4.4- and 15.1-MeV gamma-ray yields are listed in Table II and III with the corresponding values plotted in Fig. 8 and Fig. 9, respectively.

The threshold for neutron production in the $^{12}\text{C}(p,n)$ reaction is 19.64 MeV [23]. However, neutrons can also be produced below this threshold, for example from isotopic impurities such as ^{13}C in the target and from energetic gamma rays produced in the target and interacting in the surrounding materials. The presence of fast neutrons is confirmed in Fig. 3, where proton energy was below the $^{12}\text{C}(p,n)$ threshold. The results indicate that as the energy of the protons is increased, the endpoint of the light output distribution corresponding to neutrons

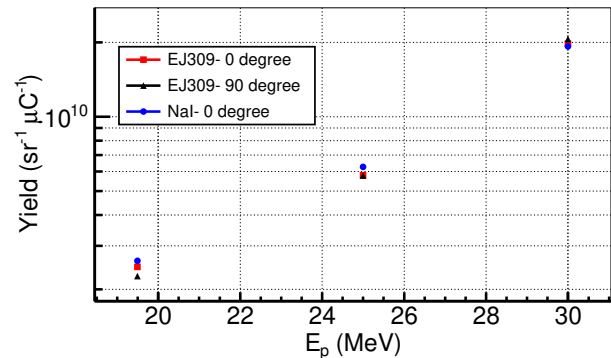


FIG. 8: Gamma-ray yields at 4.4 MeV for EJ-309 detectors and single NaI(Tl) detector at proton energies of 19.5, 25, and 30 MeV.

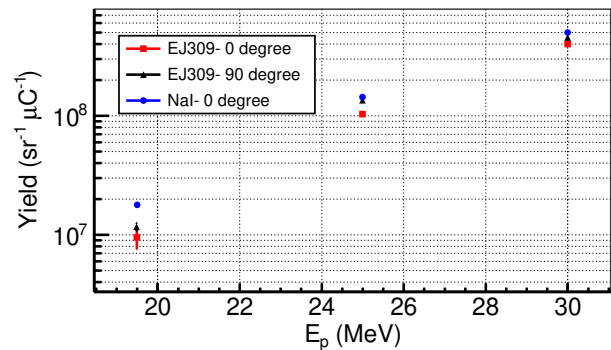


FIG. 9: 15.1-MeV gamma-ray yields for both EJ-309 detectors and single NaI(Tl) detector for proton energies of 19.5, 25, and 30 MeV.

increases, and therefore the energy of the produced neutrons also increases. Further, we observe an increase in the total number of observed neutrons with increasing incident proton energy.

TABLE II: 4.4-MeV gamma-ray yield measured with 3'' EJ-309 detector including the statistical uncertainty.

Proton Energy (MeV)	Position	Yield ($\text{sr}^{-1} \mu\text{C}^{-1}$)
19.5	0°	$2.46 \times 10^9 \pm 5.4 \times 10^6$
	90°	$2.4 \times 10^9 \pm 5.9 \times 10^6$
25	0°	$5.81 \times 10^9 \pm 9.2 \times 10^6$
	90°	$5.98 \times 10^9 \pm 1.0 \times 10^7$
30	0°	$1.57 \times 10^{10} \pm 2.4 \times 10^7$
	90°	$1.65 \times 10^{10} \pm 3.3 \times 10^7$

The photon and neutron dose equivalents are associated with the measured total readings Q_7 and Q_6 of TLD 700 and TLD 600 and are shown in Table IV. Each reading is averaged from the results of three independent chips and the uncertainty is quoted as the associated standard deviation. Because the photon flux is larger than the neutron flux in the experimental environment and the TLD 700 is much less sensitive to neutrons than TLD 600 (for neutron energy $\lesssim 10$ MeV) [28], the total

TABLE III: 15.1-MeV gamma-ray yield measured with 3" EJ-309 detector including the statistical uncertainty.

Proton Energy (MeV)	Position	Yield ($\text{sr}^{-1} \mu\text{C}^{-1}$)
19.5	0°	$8.13 \times 10^6 \pm 1.9 \times 10^6$
	90°	$2.56 \times 10^7 \pm 8.9 \times 10^5$
25	0°	$9.18 \times 10^7 \pm 3.6 \times 10^6$
	90°	$1.53 \times 10^8 \pm 1.7 \times 10^6$
30	0°	$3.44 \times 10^8 \pm 7.1 \times 10^6$
	90°	$4.47 \times 10^8 \pm 3.8 \times 10^6$

TABLE IV: Results of TLD measurements.

Proton energy (MeV)	Angle	TLD 700		TLD 600	
		Q_7 (nC)	Q_6 (nC)	$Q_{6,n}$ (nC)	
19.5	0°	8447 ± 383	8731 ± 1661	930 ± 1698	
	90°	8146 ± 889	9612 ± 2024	2090 ± 2184	
25	0°	22331 ± 4520	38724 ± 2384	18118 ± 4811	
	90°	19810 ± 927	34400 ± 4902	16105 ± 4977	
30	0°	35722 ± 1510	151812 ± 9721	118822 ± 9821	
	90°	33535 ± 1870	117670 ± 6188	86700 ± 6424	

readings Q_7 of TLD 700 are dominated by the photon response, such as $Q_7 \simeq Q_{7,p}$. Therefore, the photon dose D_{ph} listed in Table V can be estimated from Eq. (2). Following the calculation using Eqs. (3) and (4), the neutron response $Q_{6,n}$ of TLD 600 can be estimated and is listed in Table IV.

TABLE V: Estimated photon and neutron dose distributions from TLD measurements.

Proton energy (MeV)	Angle	Photon dose ($\mu\text{Gy} \mu\text{C}^{-1}$)	Neutron dose equivalent ($\mu\text{Sv} \mu\text{C}^{-1}$)
19.5	0°	13.69 ± 0.62	15.83 ± 28.92
	90°	13.19 ± 1.44	35.77 ± 37.18
25	0°	42.21 ± 8.56	359.83 ± 95.56
	90°	37.45 ± 1.76	319.83 ± 98.85
30	0°	61.39 ± 2.6	2145.27 ± 195.04
	90°	45.66 ± 2.53	1565.31 ± 127.58

When $E_p = 19.5$ MeV, TLD 600 results indicate that the neutron flux is much lower than the photon flux, so that the neutron reading $Q_{6,n}$ represents a minor component of the Q_6 response. This low neutron flux is near the detection limit of TLD 600, resulting in the significant uncertainties of the measured Q_6 and the estimated $Q_{6,n}$. When the proton energy is increased to $E_p = 25$ and 30 MeV, Q_7 and Q_6 readings also increase as a result of the increased photon and neutron flux. Note that for TLD 600, the neutron reading $Q_{6,n}$ becomes comparable to the corresponding photon reading $Q_{6,p} = Q_6 - Q_{6,n}$ for $E_p = 25$ MeV, while $Q_{6,n}$ can greatly surpass $Q_{6,p}$ with $E_p = 30$ MeV. The neutron dose equivalent H_n in Table V was evaluated using Eq. (5). The TLD data in Tables IV and V indicate a two orders of magnitude increase of the neutron dose equivalent at 0° when the proton energy is increased from 19.5 to 30 MeV; a mod-

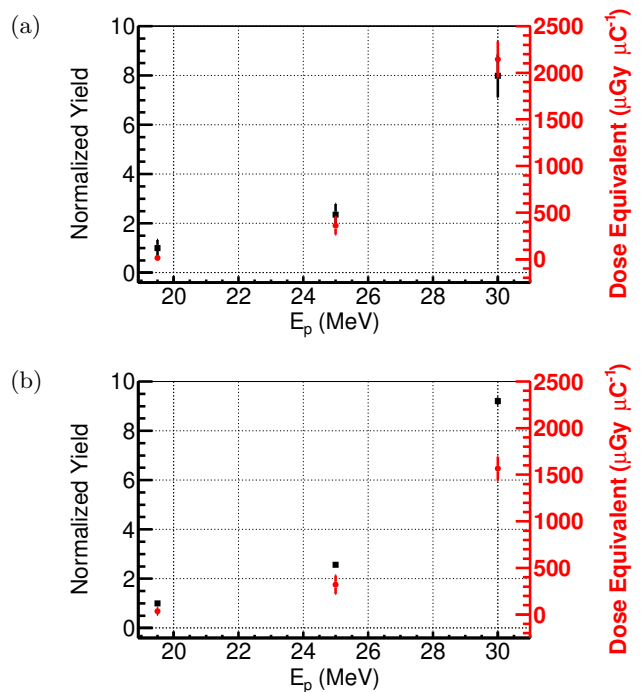


FIG. 10: 15.1-MeV gamma-ray yield normalized to the yield at $E_p=19.5$ MeV and neutron dose equivalent for incident proton energies of 19.5, 25, and 30 MeV.

Results from EJ309 detectors and TLDs are shown at (a) 0° and (b) 90°.

erate five-fold enhancement is obtained for the photon dose over the same proton energy range.

V. CONCLUSIONS

The measured current-normalized thick-target 4.4- and 15.1-MeV gamma-ray yields from $^{12}\text{C}(p,p')^{12}\text{C}$ at both 0° and 90° are greater than the previously measured $^{11}\text{B}(d,\gamma n)^{12}\text{C}$ 0° yield at the 3-MeV incident deuteron energy for all tested proton energies. The highest 15.1-MeV photon yield was measured at a proton energy of 30 MeV at 90°, and represents a 72.1-factor increase over $^{11}\text{B}(d,\gamma n)^{12}\text{C}$ at 0°. The photon dose measurements show increases in photon dose which are nearly commensurate with the increase in the measured 4.4-MeV gamma-ray yield as the proton energy is increased. Figure 10 shows the gamma-ray yield normalized to the yield at $E_p = 19.5$ MeV and neutron dose, at three proton energies used in the experiment. Unlike the photon dose, the neutron dose increases at a rate much greater than the 15.1-MeV photon yield as the proton energy is increased in the range of 19.5–30 MeV. There is a two orders of magnitude increase of the neutron dose when the proton energy is raised from 19.5 MeV to 30 MeV, while a factor of approximately five is observed for the photon dose over the same proton energy range. Increasing the proton energy up to 30 MeV results in increases of gamma-ray

yields, but these are outpaced by the increases in neutron dose.

An AI system for cargo scanning of sea-going containers based on the $^{12}\text{C}(\text{p},\text{p}')^{12}\text{C}$ reaction could potentially address some of the key technical specifications required for new AI systems [9]. By taking advantage of the emission of the gamma rays into a large solid angle, even multiple cargo scanning streams may be feasible with a single source, thereby increasing the container throughput. With no direct neutron production at proton energies below 19.5 MeV, the $^{12}\text{C}(\text{p},\text{p}')^{12}\text{C}$ reaction should further reduce the neutron shielding requirements and lower the total radiation dose imparted to cargo or stowaways [17]. The reduction in the amount of required shielding would also reduce the overall geometric footprint of the system – another important specification. The gamma-ray energies produced by this reaction would provide higher penetration capability than existing bremsstrahlung systems (6- and 9-MeV photon energy endpoints) while enabling

robust material discrimination by means of dual-energy photon radiography [12, 13].

ACKNOWLEDGMENTS

The authors wish to thank Paul Rose and Anna Erickson for assistance with the CoPASS data acquisition package. This work was supported by the US Department of Homeland Security [2015-DN-077-ARI096]. The research of J.N. was performed under appointment to the Nuclear Nonproliferation International Safeguards Fellowship Program sponsored by the National Nuclear Security Administrations Office of International Safeguards (Grant No. NA-241). The research of F.S. was performed under appointment to the Livermore Graduate Scholar Program Fellowship.

-
- [1] R. Kouzes, Detecting illicit nuclear materials: The installation of radiological monitoring equipment in the united states and overseas is helping thwart nuclear terrorism, *Am. Sci.* **93**, 422 (2005).
- [2] R. Runkle, L. Smith, and A. Peurrung, The photon haystack and emerging radiation detection technology, *J. Appl. Phys.* **106**, 7 (2009).
- [3] C. Grassley, M. Baucus, B. Thomas, and C. Rangel, in *General Accounting Office, US Congress, GAO-03-770* (2003).
- [4] M. Thibault, M. Brooks, and K. Button, The response of the us maritime industry to the new container security initiatives, *Transportation Journal*, 5 (2006).
- [5] I. Jovanovic and A. Erickson, *Active Interrogation in Nuclear Security: Science, Technology and Systems* (Springer, 2018).
- [6] C. Geddes, B. Ludewigt, J. Valentine, B. Quiter, M.-A. Descalle, G. Warren, M. Kinlaw, S. Thompson, D. Chichester, C. Miller, *et al.*, *Impact of Monoenergetic Photon Sources on Nonproliferation Applications Final Report*, Tech. Rep. (Idaho National Lab.(INL), Idaho Falls, ID (United States), 2017).
- [7] J. Jones, J. Sterbentz, W. Yoon, and D. Norman, in *AIP Conference Proceedings*, Vol. 1194 (AIP, 2009) pp. 43–48.
- [8] C. Liu, G. Golovin, S. Chen, J. Zhang, B. Zhao, D. Haden, S. Banerjee, J. Silano, H. Karwowski, and D. Umstadter, Generation of 9 mev γ -rays by all-laser-driven compton scattering with second-harmonic laser light, *Opt. Lett.* **39**, 4132 (2014).
- [9] W. C. Organization, Guidelines for the procurement and deployment of scanning/NII equipment, Tech. Rep. (2015).
- [10] J. Nattress, *Discriminating Materials Using a Multiparticle Approach in an Active Interrogation Environment*, Ph.D. thesis, University of Michigan (2018).
- [11] T. Taddeucci, R. Sheffield, T. Massey, D. Carter, J. ODonnell, C. Brune, D. Ingram, D. Jacombs, and A. DiLullo, Neutron and gamma-ray production with low-energy beams, Los Alamos National Laboratories Report LA-UR-07-2724 (2007).
- [12] P. Rose, A. Erickson, M. Mayer, J. Nattress, and I. Jovanovic, Uncovering special nuclear materials by low-energy nuclear reaction imaging, *Sci. Rep.* **6** (2016).
- [13] B. Henderson, H. Lee, T. MacDonald, R. Nelson, and A. Danagoulian, Experimental demonstration of multiple monoenergetic gamma radiography for effective atomic number identification in cargo inspection, *J. Appl. Phys.* **123**, 164901 (2018).
- [14] J. Nattress, T. Nolan, S. McGuinness, P. Rose, A. Erickson, G. Peaslee, and I. Jovanovic, High-contrast material identification by energetic multiparticle spectroscopic transmission radiography, *Phys. Rev. Applied* **11**, 044085 (2019).
- [15] M. Mayer, J. Nattress, and I. Jovanovic, Detection of special nuclear material from delayed neutron emission induced by a dual-particle monoenergetic source, *Appl. Phys. Lett.* **108**, 264102 (2016).
- [16] J. Nattress, K. Ogren, A. Foster, A. Meddeb, Z. Ounaies, and I. Jovanovic, Discriminating uranium isotopes using the time-emission profiles of long-lived delayed neutrons, *Phys. Rev. Applied* **10**, 024049 (2018).
- [17] T. Taddeucci, High-energy gamma rays from $^{12}\text{C}(\text{p},\text{p}')$, Tech. Rep. (Los Alamos National Lab.(LANL), Los Alamos, NM (United States), 2011).
- [18] M. Chadwick, P. Obložinský, M. Herman, N. Greene, R. McKnight, D. Smith, P. Young, R. MacFarlane, G. Hale, S. Frankle, *et al.*, ENDF/B-VII. 0: next generation evaluated nuclear data library for nuclear science and technology, *Nucl. Data Sheets* **107**, 2931 (2006).
- [19] F. Ajzenberg-Selove, Energy levels of light nuclei $a = 1112$, *Nucl. Phys. A* **506**, 1 (1990).
- [20] E. K. Warburton and H. O. Funsten, High-Energy Gamma Rays and Low-Energy Protons and Deuterons from $\text{C}^{12} + \text{p}$ for $E_p=14\text{-}20$ MeV, *Phys. Rev.* **128**, 1810 (1962).
- [21] D. Measday, P. Fisher, A. Kalmykov, F. Nikolaev, and A. Clegg, The $^{12}\text{C}(\text{p}, \text{p})^{12}\text{C}$ (12.71 and 15.11 mev) reaction from threshold to 50 mev, *Nucl. Phys.* **45**, 98 (1963).

- [22] R. H. Howell, F. S. Dietrich, D. W. Heikkinen, and F. Petrovich, $(p,p'\gamma)$ spin-flip measurement for 1^+ states in ^{12}C at $E_p = 23.5 - 27$ mev, *Phys. Rev. C* **21**, 1153 (1980).
- [23] E. Rimmer and P. Fisher, Resonances in the (p,n) reaction on ^{12}C , *Nucl. Phys. A* **108**, 561 (1968).
- [24] D. Berghofer, M. Hasinoff, R. Helmer, S. Lim, D. Measday, and K. Ebisawa, High-energy levels in ^{13}N (II), *Nuclear Physics A* **263**, 109 (1976).
- [25] Eljen Technologies, Neutron/Gamma PSD Liquid Scintillator Data Sheet EJ-301, EJ-309, (Date Accessed: Apr 22, 2017).
- [26] CoMPASS User Manual UM5960, (2018).
- [27] J. Nattress and I. Jovanovic, Response and calibration of organic scintillators for gamma-ray spectroscopy up to 15-MeV range, *Nucl. Instrum. Methods Phys. Res., Sect. A* **871**, 1 (2017).
- [28] F. Hsu, M. Chiu, Y. Chang, C. Yu, and H. Liu, Estimation of photon and neutron dose distributions in the THOR BNCT treatment room using dual TLD method, *Radiat. Meas.* **43**, 1089 (2008).
- [29] S. Agostinelli *et al.*, Geant4—simulation toolkit, *Nucl. Instrum. Methods Phys. Res., Sect. A* **506**, 250 (2003).
- [30] R. Brun and F. Rademakers, ROOT — An object oriented data analysis framework, *Nucl. Instrum. Methods Phys. Res., Sect. A* **389**, 81 (1997).